A semi-idealized modeling study on the long-lived eastward propagating mesoscale convective system over the Tibetan Plateau

Shenming FU[1,2*], Zi MAI[2,3], Jianhua SUN[2,4], Wanli LI[5], Qi ZHONG[5], Jiaren SUN[6] & Yuanchun ZHANG[2,4]

[1] *International Center for Climate and Environment Sciences, Institute of Atmospheric Physics, Chinese Academy of Sciences, Beijing 100029, China;*
[2] *Heavy Rain and Drought-Flood Disasters in Plateau and Basin Key Laboratory of Sichuan Province, Chengdu 610225, China;*
[3] *National Meteorological Center of China Meteorological Administration, Beijing 100081, China;*
[4] *Key Laboratory of Cloud-Precipitation Physics and Severe Storms, Institute of Atmospheric Physics, Chinese Academy of Sciences, Beijing 100029, China;*
[5] *China Meteorological Administration Training Center, Beijing 100081, China;*
[6] *Key Laboratory of Urban Ecological Environmental Simulation and Protection of Ministry of Environmental Protection, South China Institute of Environmental Sciences, the Ministry of Environmental Protection of China, Guangzhou 501530, China*

Abstract   Based on a 16-warm-season statistical study on the mesoscale convective systems (MCSs) that were generated over the Tibetan Plateau (TP), 11 long-lived eastward propagating MCSs of the same type were selected for a composite semi-idealized simulation and a corresponding no-latent-heating sensitivity run by using the Weather Research and Forecasting (WRF) model. Common evolutionary features and associated mechanisms of this type of long-lived eastward propagating MCS were investigated. Main results are as follows: (i) This type of MCS was generated in a favorable background environment which was characterized by a notable upper-tropospheric divergence south of an upper-level jet, a strong warm advection around a middle-level shortwave trough's central area, and an instable convective stratification below the trough. Development of the MCS featured rapid increase of cyclonic vorticity in the middle and lower troposphere. The convergence-related vertical stretching and tilting were key factors for the cyclonic-vorticity's production, and convection-related upward cyclonic-vorticity transport contributed to the upward extending of the MCS. (ii) During the vacating stage of the MCS, it first coupled with a quasi-stationary Tibetan Plateau vortex (TPV) over the TP's eastern section, and then decoupled from the vortex. In the former stage, the MCS contributed to maintaining ascending motions and convergence associated with the TPV, which favored its persistence; whereas, in the latter stage, decoupling weakened the TPV-associated convection significantly. This reduced the upward transport of cyclonic vorticity notably, which, together with the negative tilting effect, finally led to the vortex's dissipation. (iii) After vacating TP, the MCS first weakened due to the disappearance of strong direct sensible heating from the TP on its bottom, and then, under the favorable conditions associated with the shortwave trough over the eastern section of the TP, the MCS redeveloped rapidly. Convergence-related cyclonic-vorticity production in the middle and lower troposphere and upward transport of cyclonic vorticity due to convection governed the MCS's redevelopment. (iv) Sensitivity simulation shows that latent heating was a necessary condition for the formation and development of the long-lived eastward propagating MCS. On the one hand, this MCS affected the TP's eastern section and downstream regions directly by inducing precipitation; and on the other hand, it exerted effects on the precipitation over a wider range in the downstream regions by modulating large-scale circulations over and around the TP.

Keywords   Tibetan Plateau, Mesoscale convective system, Tibetan Plateau vortex, Heavy rainfall, Vorticity budget, Sensitivity simulation

---

* Corresponding author (email: fusm@mail.iap.ac.cn)

1.   Introduction

Known as the "third pole in the world", the Tibetan Plateau (TP) accounts for ~25% of China's total land area and has a mean altitude of more than 4000 m. It is the largest, highest and steepest plateau in the Northern Hemisphere, which features very complex topography. On average, the topography of the TP is higher in its western section and decreases eastwards. Affected by the Asian monsoon and the Eurasian subtropical high, the TP shows its unique features in weather and climate. Because the altitude of the TP is notably higher than that of the regions at similar latitudes, the plateau exerts a continuous dynamic effect on the atmospheric circulation. Affected by this, the westerly wind shows three main motion types: one air-current branch is forced to climb along the western section of the plateau; and the other two branches mainly go around the TP along its northern and southern edges, which result in a ridge/trough north/south of the TP (Ye and Gao, 1979; Ding, 2005). Thermodynamic forcing of the TP is also remarkable, which is characterized by notable seasonal variations (Yanai et al., 1992; Li and Xu, 2005; Liu et al., 2020). Overall, TP's thermodynamic forcing reaches maxima in summer and winter. For summer, under the influence of strong solar radiation, the TP acts as a huge heat source, which results in a stable strong anticyclone in the upper troposphere and a strong cyclonic circulation zone in the middle troposphere (Yang et al., 1992; Ding, 2005). Under this favorable background environment, convective activities are notably vigorous over the TP, with 20–50 mature convective clouds appeared over 10,000 square kilometers on average (Flohn and Reiter, 1968).

Under advantageous conditions, convective clouds over the TP can be further organized to form a larger-scale system —the mesoscale convective system (MCS). The MCS is a cloud system that occurs in connection with an ensemble of thunderstorms and produces a contiguous precipitation zone on the order of ≥100 km in the horizontal scale in at least one direction (https://glossary.ametsoc.org/wiki/Mesoscale_convective_system). In warm seasons, MCSs frequently appeared over the TP (Zhu and Chen, 1999; Zheng et al., 2008), which contributed more than 70% to the total accumulated precipitation in some regions of the plateau (Li et al., 2008; Hu et al., 2016, 2017; Mai et al., 2021). According to Mai et al. (2021), ~70% of the MCSs (that were generated over the TP) lasted for a period of less than 6 h, with most of them dissipating over the plateau. Only a small proportion of the MCSs had relatively long lifespans, with some of them

moving eastward and vacating the TP (these are defined as the eastward-moving and vacating type (EVT) of MCS) under favorable background circulations (Zhuo et al., 2002; Mai et al., 2021). After vacating the TP, the EVTs could interact with the weather systems along their tracks (Fu et al., 2019), and sometimes they could induce torrential rainfall events that resulted in severe floods. For instance, the catastrophic floods over the Yangtze River Basin (1998) and Huaihe River Basin (2003 and 2007) were all closely related to the EVTs' eastward displacement and development (Zhao et al., 2004; Fu et al., 2011).

Due to their great ability in causing severe disastrous weather, the EVTs had long been a research focus for scholars at home and abroad. For instance, Yi and Xu (2001) investigated the EVTs during the flood season of 1998 and found that EVTs could induce heat and moisture transport to downstream regions, which served as favorable conditions for torrential rainfall events there. The comprehensive analysis by Zhang and Tao (2002) showed that when the EVTs over the TP, the cold air in the middle and high latitudes, the subtropical high over the Northwest Pacific, and the monsoon surge in the South China Sea were all in their active stages, it is easy to form a series of heavy rainfall events that caused severe floods in a large area. Yasunari and Miwa (2006) and Fu et al. (2010) investigated torrential rainfall events that were induced by EVTs, and their results indicated that southwest vortices sometimes appeared during the EVTs' vacating stages, which enhanced the precipitation intensity notably. Fu et al. (2011) focused on the EVTs in the Meiyu seasons of 2003 and 2007, and classified them into four categories. Of these, the category featured an EVT and an associated eastward moving middle-tropospheric convergent center, which exerted the largest effects on the precipitation in downstream regions. Hu et al. (2016) conducted a composite study on EVTs and found that the location and intensity of the upper-level jet were important to their displacement. Based on a 16-warm-season (from May to September) statistical study on MCSs over the TP, Mai et al. (2021) found that of the ~10,000 detected MCSs, only ~6.6% could move out from the TP. These EVTs accounted for 20% of the short-duration heavy precipitation (precipitation ≥20 mm per hour) in some regions around the Sichuan Basin.

In summary, previous studies have confirmed the importance of EVTs to the precipitation over the regions east of the TP. They also highlighted that MCSs of different types had distinctive evolutionary characteristics and different impacts on the downstream precipitation. A statistical result from Mai et al. (2021) showed that, of the total ~10000

detected MCSs, only ~3.3% could last for 3 h or more after they vacated the TP (~50% of the total EVTs). These relatively long-lived EVTs could last for a longer period, affect a broader range, and induced heavier precipitation. However, thus far, only few studies focused on the development and maintenance mechanisms of this type of EVTs, which were mainly from the viewpoint of case study. Therefore, the common characteristics of the long-lived EVTs are far to be well understood. For that, based on the 16-warm-season statistical result from Mai et al. (2021), we first selected typical long-lived EVTs of the same type and then composited them to drive the Weather Research and Forecasting (WRF) model for a composite semi-idealized simulation and a corresponding no-latent-heating (NOLH) sensitivity run. Analyses and dynamical diagnoses were conducted on the simulation results to show the common evolutionary characteristics and associated mechanisms of the long-lived EVTs, which is helpful to further the understanding of this type of MCSs.

2. Data and method

2.1 Data

The Climate Forecast System Reanalysis (CFSR) (Saha et al., 2014) provided by the National Centers for Environmental Prediction (NCEP) was used in this study for the composite analyses, semi-idealized composite simulations, and simulation validation. The data has a temporal resolution of 6-h, a spatial resolution of 0.5°×0.5°, and a total of 37 vertical levels. In addition, the 30-min 0.0727°×0.0727° CMORPH precipitation estimate data (Joyce et al., 2004) was used for verification of the precipitation simulation.

2.2 Method

2.2.1 Selection of long-lived EVTs of the same kind

Typical EVTs of the same type were composited for the semi-idealized simulation used in this study. A shown in Table 1, a total of 11 EVTs was utilized in the composite, which were selected as follows: (i) According to the ranges affected by the EVTs, Region I (26°–40°N, 80°–126°E), Region II (12°–26°N, 80°–126°E), and Region III (40°–54° N,80°–126°E) were determined. Regions I–III were mainly affected by the eastward-moving, southeastward moving, and northeastward moving EVTs (Hu et al., 2016; Mai et al., 2021), with Region I having the largest frequency of EVTs. (ii) Based on the statistical result from Mai et al. (2021), we selected the EVTs (those cases affected by typhoons were not considered) with relatively long lifespans (this contains a total of 251 EVTs). A 12-h temporal mean (from 6 h before an EVT's formation to 6 h after its formation) of the 500-hPa geopotential height field associated with each EVT was

calculated (defined as M_i, where i stands for the number of the EVT), which was then composited for all the 251 EVTs (defined as M_a). It is clear that M_i and M_a represent the mean feature (of the 500-hPa geopotential height) of EVT i and all 251 EVTs, respectively. (iii) Calculated the deviation of M_i from M_a (defined as D_i), which can represent the smaller-scale features associated with EVT i. (iv) Correlation calculations (using D_i) between each EVT with the remaining 251 EVTs were calculated within Regions I–III, respectively. For the EVT i, we counted the number of times (define as N_i) that it satisfied two conditions (*a.* its correlations with other EVTs were ≥ 0.7 within Region I, which ensures it had similar influencing systems to those of other EVTs within Region I; *b.* its correlations with other EVTs were ≥0 within Regions II and III, which ensures its influencing systems were not in an opposite phase with those of other EVTs within Regions II and III) at the same time. Compared EVT-i's N_i with those of others, and thus determined the one (suppose it was EVT l) had the largest number of times (that it satisfied the two conditions *a* and *b*). (v) After the EVT l was determined, we used another two conditions to only focus on long-lived EVTs: (1) Its life span must be ≥12 h, and (2) after vacating the TP, it must last for at least 6 h. After processing the EVTs by using (i)–(v), a total of 11 EVTs (Table 1) were selected for the semi-idealized simulation.

2.2.2 Model configuration of the semi-idealized simulation

The WRFv3.8 (Skamarock et al., 2008) was used in this study for all simulations. The composite semi-idealized simulation used three domains (Figure 1a) with one-way nesting. Horizontal resolutions of d01–d03 were 36 km (331×241 grid points), 12 km (541×343 grid points), and 4 km (1141×721 grid points), respectively. There was a total of 51 vertical levels, with the model top fixed at 50 hPa. The planetary boundary layer scheme of Yonsei University (YSU; Noh et al., 2001), the WRF single-moment 6-class (WSM6) microphysics scheme (Hong and Lim, 2006), the

Table 1 The 11 MCS cases used for the semi-idealized simulation

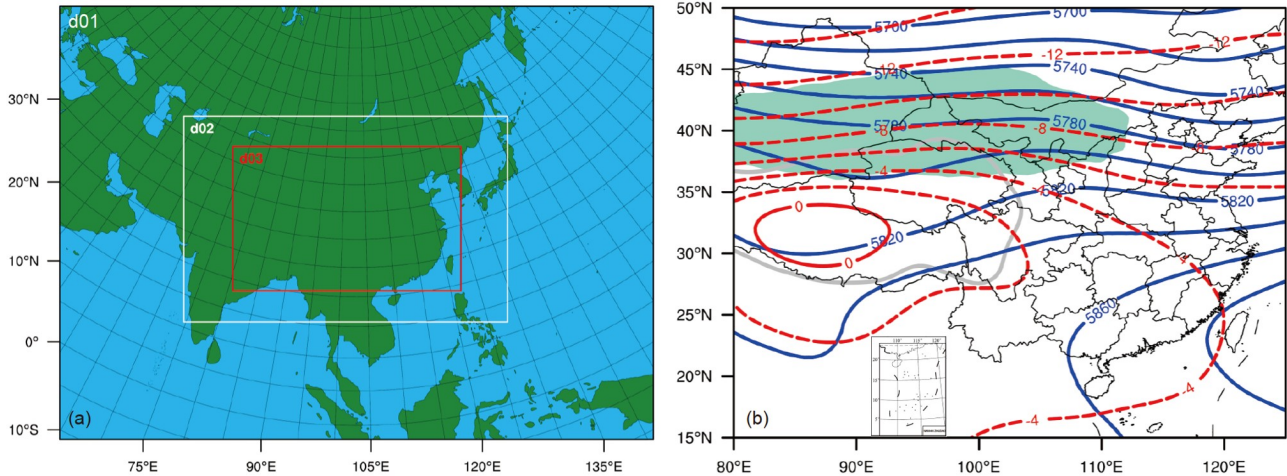| No.	Formation time (UTC)	Dissipation time (UTC)	Life span (h)
1	2003062908	2003063011	27
2	2003092510	2003092600	14
3	2004081916	2004082012	20
4	2006082708	2006082804	20
5	2008061811	2008061913	26
6	2008062909	2008063011	26
7	2009073007	2009073109	26
8	2011081508	2011081523	15
9	2012070607	2012070711	28
10	2013082708	2013082805	21
11	2014062407	2014062504	21

Figure 1 Configurations of the nested three domains for the simulations (a), and the initial field of the control run (b), where blue solid lines represent 500 hPa geopotential height (units: gpm), red dashed lines show 500 hPa temperature (units: °C), and green shading shows the area where 200 hPa wind speed exceeds 30 m s^{-1}.

Noah land-surface model (Chen and Dudhia, 2001), the RRTM long-wave radiation scheme (Mlawer et al., 1997), and the Dudhia shortwave radiation scheme (Dudhia, 1989) were used in d01–d03. The Kain-Fritsch (KF) cumulus parameterization scheme (Kain, 2004) was only utilized in d01–d02 (d03 had no cumulus parameterization scheme, as it was convection permitting). In this study, all analyses and calculations used the simulation result from d03, except for large-scale background environment (e.g., Figure 1b), which used the output of d01.

The initial and boundary conditions for the composite semi-idealized simulation were determined as follows: suppose $t=0$ represents the time when EVT i formed (temporal resolution of CFSR data is 6 h). For a variable V (e.g., wind field, geopotential height, etc.) that need to be composited, the series $V_i(t=-3)$, $V_i(t=-2)$, $V_i(t=-1)$, $V_i(t=0)$, $V_i(t=1)$, $V_i(t=2)$, $V_i(t=3)$, $V_i(t=4)$, $V_i(t=5)$, $V_i(t=6)$ stand for the time series from 18 h before EVT-i' formation to 36 h after its generation (as Table 1 shows, the largest lifespan of the 11 EVTs was 28 h). Based on the Eulerian viewpoint, variables associated with the 11 EVTs were composited equally weighted, which resulted in an idealized time series (from $t=-3$ to $t=6$). This time series was used to generate the initial and boundary conditions for the semi-idealized simulation (Fu et al., 2017). As most of the EVTs used in composite was generated in 07:00–09:00 UTC, we started the simulation at 12:00 UTC (as 06:00 UTC was the closest time to the mean formation time of the 11 EVTs, when we started the simulation 18 h earlier, it was 12:00 UTC in the previous day). The initial field for the simulation is shown in Figure 1b. The semi-idealized composite simulation was defined as the control run of this study, and a NOLH sensitivity run was also conducted. In the NOLH run, we shut down the condensation latent heating within the purple dashed box of Figure 2.

2.2.3   Vorticity budget

The vorticity budget equation was used to investigate the evolutionary mechanisms of the EVT and a Tibetan Plateau vortex (TPV). From Kirk (2003) and Fu et al. (2013, 2017), its expression is

$$\frac{\partial \zeta}{\partial t} = -\mathbf{V}_h \cdot \nabla_h \zeta - \omega \frac{\partial \zeta}{\partial p} + \mathbf{k} \cdot \left(\frac{\partial \mathbf{V}_h}{\partial p} \times \nabla_h \omega \right)$$
$$- \beta v - (\zeta + f) \nabla_h \cdot \mathbf{V}_h + \text{RES}, \qquad (1)$$

where ζ is the relative vorticity (vorticity for short and hereinafter the same), $\mathbf{V}_h = u\mathbf{i} + v\mathbf{j}$ represents the horizontal wind vector, ($\mathbf{i}$, $\mathbf{j}$, $\mathbf{k}$) are the unit vectors in the east, north and zenith directions, respectively. $\nabla_h = \frac{\partial}{\partial x}\mathbf{i} + \frac{\partial}{\partial y}\mathbf{j}$ is the gradient vector (calculated by using the central difference scheme), ω is the vertical velocity under pressure coordinate, p is the pressure, f is the Coriolis parameter, $\beta = \partial f / \partial y$, and the subscript "$h$" means the horizontal component. Terms HAV and VAV (the first and second terms on the right-hand side of eq. (1), respectively) stand for horizontal and vertical advection of vorticity, respectively; TIL (the third term on the right-hand side) denotes the vorticity variation due to tilting; AP (the fourth term on the right-hand side) is the advection of planetary vorticity (it is at least one order of magnitude smaller than other terms); STR (the fifth term on the right-hand side) is the vorticity variation caused by vertical stretching/shrinking, and RES (the last term on the right-hand side) is the residual term, which is mainly due to subgrid processes, friction and calculation errors. A total (TOT) term is defined as the sum of all terms on the right-hand side of eq. (1) except for RES: TOT=HAV + VAV + TIL + AP + STR. A check of the balance of eq. (1) by using the 15-min WRF output indicated that, after neglecting RES, the ratio of TOT to the temporal derivative on the left-hand side of eq. (1) was between 1.07 and 1.23 (not shown). This means that
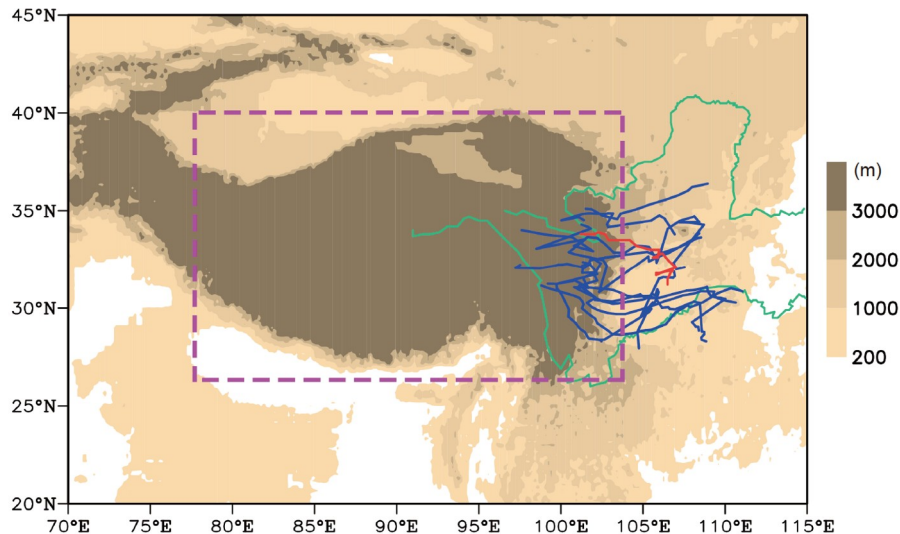
Figure 2   Tracks of the 11 selected EVTs used for the semi-idealized simulation (blue solid lines) and the control-run simulated EVT's track (red solid line), where the shading shows terrain (units: m), and the purple dashed box marks the region for sensitivity simulation.

the balance of the left and right sides of the vorticity budget equation was good, and thus the results could be used for further analyses.

3. Simulation verification and an overview of the event

3.1   Simulation verification

The composite semi-idealized simulation produced a long-lived EVT which formed at t=18.5 h (i.e., the simulation had run for 18.5 h). The corresponding time was 06:30 UTC, which was ~0.5 h later than the mean formation time of the 11 EVTs (Table 1). From Figure 2, the simulated EVT was generated around 34°N, 101.5°E, which was 1.5° latitude north and 1.5° longitude east of the 11 EVTs' mean formation location. After formation, the EVT moved eastward with time and vacated the TP, with its track captured the key features of the 11 EVTs' mean track (Figure 2). The simulated EVT had dissipated at t=47 h around 32°N, 107°E, which was close to the 11 EVTs' mean dissipation latitude, but it was ~1.5° longitude west of their mean dissipation longitude. The simulated EVT lasted for ~28.5 h, which was longer than the mean lifespan of the 11 EVTs.

A comparison between the CFSR composite background circulation with the simulated background circulation shows that: (i) In the stage before the EVTs' formation, the simulation had reasonably reproduced the location and intensity of the 200-hPa upper-level jet over the TP (Figure 3a, 3b). It also well reproduced the 500-hPa shortwave trough over the TP and the West Pacific subtropical high near the southeast coast of China. However, for the 500-hPa warm center over the western section of the TP, the simu-

lation underestimated the real situation notably. (ii) During the EVT's maintaining stage, the simulation captured the key characteristics of the upper-level jet between 35°–45°N, the 500-hPa shortwave trough east of the TP, the trough over the Bay of Bengal, and the subtropical high over the western Pacific Ocean (Figure 3c, 3d). (iii) After the EVT's dissipation, the simulation well reproduced the upper-level jet, the middle-level straight westerly flow over the TP, and the subtropical high near the southeast coast of China (Figure 3e, 3f). However, it notably underestimated intensity of the 500-hPa warm center (28°–34°N, 82°–92°E) over the western section of the TP.

For the accumulated precipitation during the EVT's whole life span, the simulated accumulated precipitation was located north of the 11 EVTs' mean accumulated precipitation (Figure 4). This is consistent with the phenomenon that the simulated EVT's track was north of the 11 EVTs' mean track. For the 11 EVTs used in the composite semi-idealized simulation, their intensities and background forcings were different from each other. When we composited them equally weighted, the composite result will be determined more by those EVTs with stronger intensities and background forcings. Therefore, the simulated EVT would show more features related to those EVTs with stronger features. This is a key reason for the difference between the semi-idealized simulation and the 11 EVTs' composite. Overall, the simulated rain band was mainly oriented in the southwest-northeast direction, and the EVT-associated precipitation was much heavier over the regions east of the TP than that over the TP (Figure 4). These were consistent with the key characteristics of the precipitation associated with the 11 EVTs.
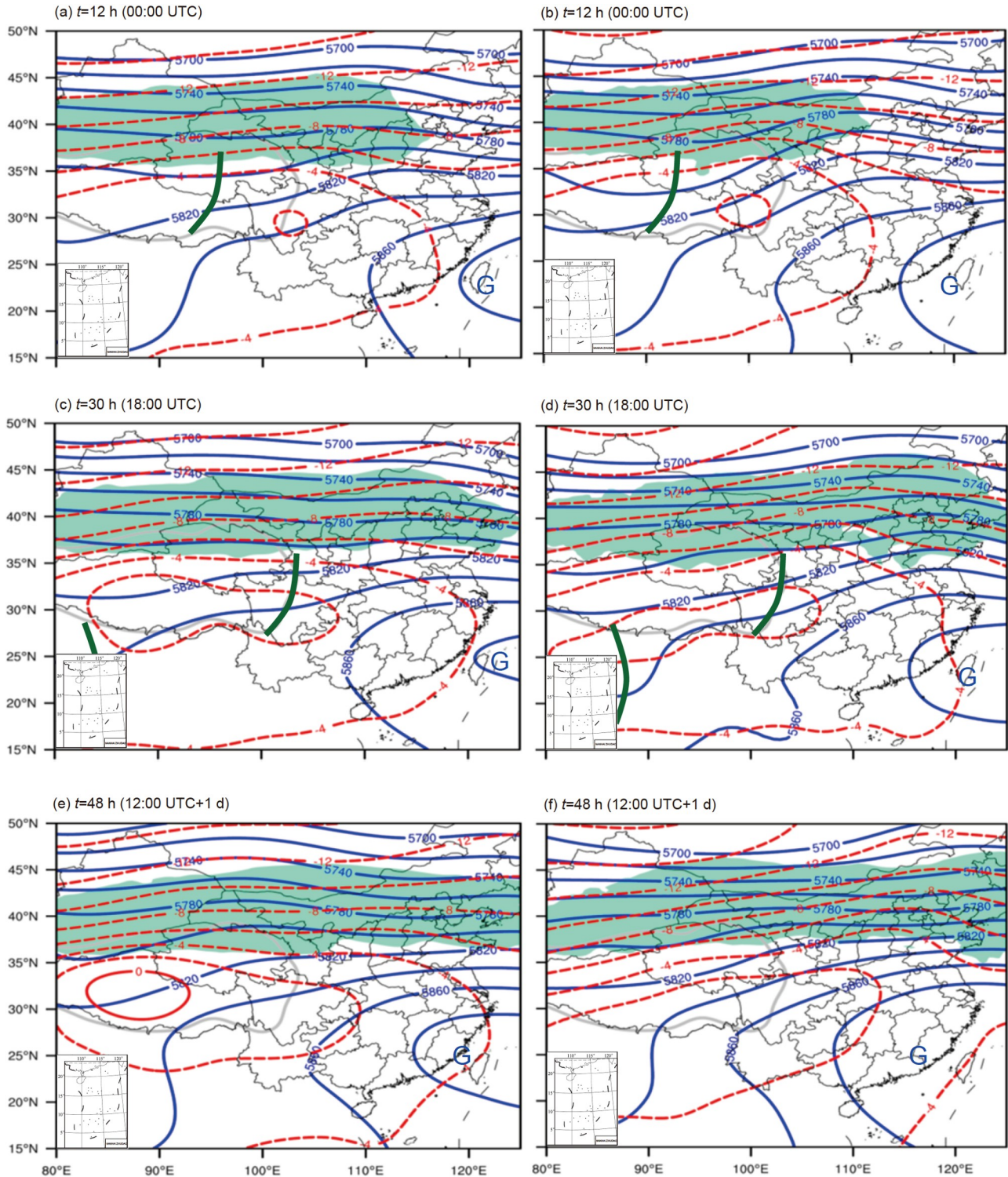
In summary, although the semi-idealized simulation

Figure 3 Composite ((a), (c), (e)) and control-run simulated ((b), (d), (f)) circulations, where blue solid lines are 500 hPa geopotential height (units: gpm), red dashed lines show 500 hPa temperature (units: °C), shading denotes the area where 200 hPa wind speed exceeded 30 m s^{-1}, thick green sold lines are trough lines, and "G" marks the subtropical high.

showed some different features from those of the 11 EVTs' composite (e.g., the simulated formation location, track and rainband of the EVT were located in regions with larger latitudes, etc.), the simulation had reasonably reproduced key characteristics of the 11 EVTs' background circulations, tracks, evolution and precipitation. Therefore, the simulated EVT could be used as a representative for a further study on this type of EVT.
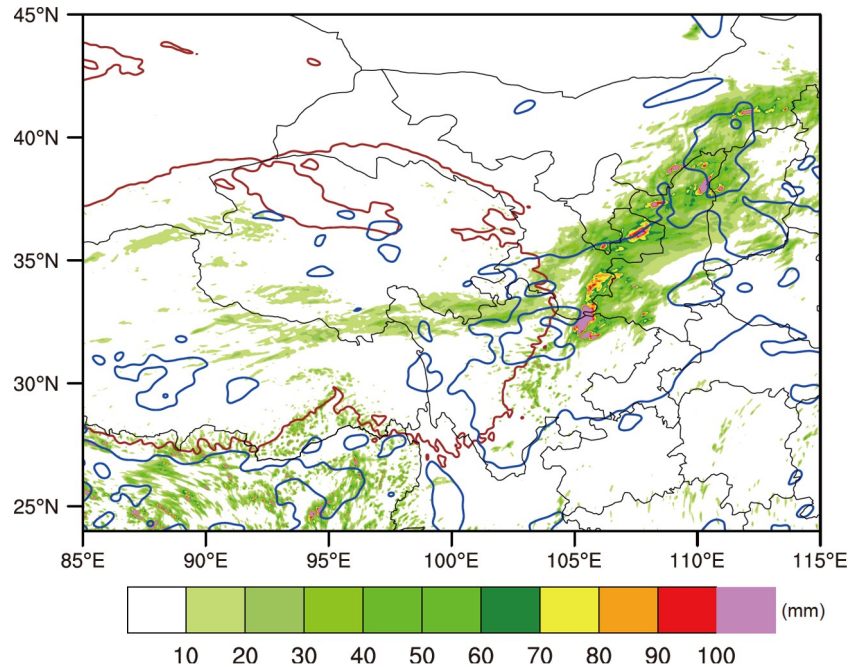
Figure 4 The control-run simulated accumulated precipitation (shading, units: mm) associated with the EVT during its whole lifespan (from *t*=18.5 h to 47 h), and the mean accumulated precipitation of the 11 EVTs during their respective lifespans where precipitation exceeded 50 mm (blue lines), where the brown line shows the terrain above 3,000 m.

3.2   Overview of the simulated event

At *t*=17 h (05:00 UTC), convective clouds appeared around 34°N, 101°E, with their minimum TBB (temperature of black body) lowering below −52°C. In this stage, coverage of these convective clouds was small. In the following 1.5 h, affected by the shortwave trough over the TP (Figure 6a), the convective clouds developed rapidly (represented by the lowering TBB and enlarging coverage) and moved eastward under the steering of strong westerly flow (Figure 5a, 5d). By *t*=18.5 h (06:30 UTC), coverage of their cold cloud (TBB< −52°C) area exceeded 5000 km^2 (Figure 5d), which satisfied the lower limit of an MCS's area condition (Zheng et al., 2008; Mai et al., 2021). Therefore, the EVT formed.

From *t*=18.5 h to 21 h, the shortwave trough over the eastern section of the TP enhanced (Figure 6a, 6b), with the EVT embedded in its central area. As the configuration of temperature and wind fields shows, the EVT was governed by warm advection, which was conducive to its development. In this stage, the EVT kept moving eastward, with its coverage enlarged rapidly and intensity enhanced notably. At around *t*=21 h, the EVT merged several newly born convective clouds west of it, and then presented a clear linear structure (Figures 5e and 6b). In this stage, the EVT showed a minimum TBB of below −80°C, which indicates that it was strong in intensity. Under the steering of the strong westerly wind associated with the shortwave trough over the eastern section of the TP (Figure 6a–6c), the EVT began to vacate the TP around *t*=24 h. In the meanwhile, newly born con-

vective clouds appeared in the regions immediately east of the TP (Figure 5f). These new convective clouds were merged by the EVT, which favored the EVT's maintenance after its vacating. From *t*=24 h on, main body of the EVT started to vacate the TP, and by *t*=29 h, the EVT had completely moved out from the TP (Figure 6c, 6d). During the vacating process, the EVT first weakened, with its intensity and coverage both decreased. From *t*=30 h to 33 h, under the favorable conditions ahead of the shortwave trough over the eastern section of the TP, the EVT merged with several newly born convective clouds northeast of it and enhanced again rapidly (Figure 6e, 6f). In this stage, its minimum TBB lowered to below −76°C (its height was around 100 hPa). A southwest-northeast oriented strong wind band appeared within the EVT, which resulted in a notable warm advection ahead of the shortwave trough. The warm advection was a favorable condition for the EVT's sustainment. By *t*=38 h, coverage and intensity of the EVT reached their respective maxima again mainly due to its merging with newly born convective clouds. Then, the EVT weakened with time, and finally, it dissipated at *t*=47 h (not shown).

4.   Evolutionary features and associated mechanisms of the EVT

4.1   Formation stage

As section 3.2 shows, the simulated EVT formed within the box 33°–35°N, 101°–103°E (Figure 5d), and thus we defined
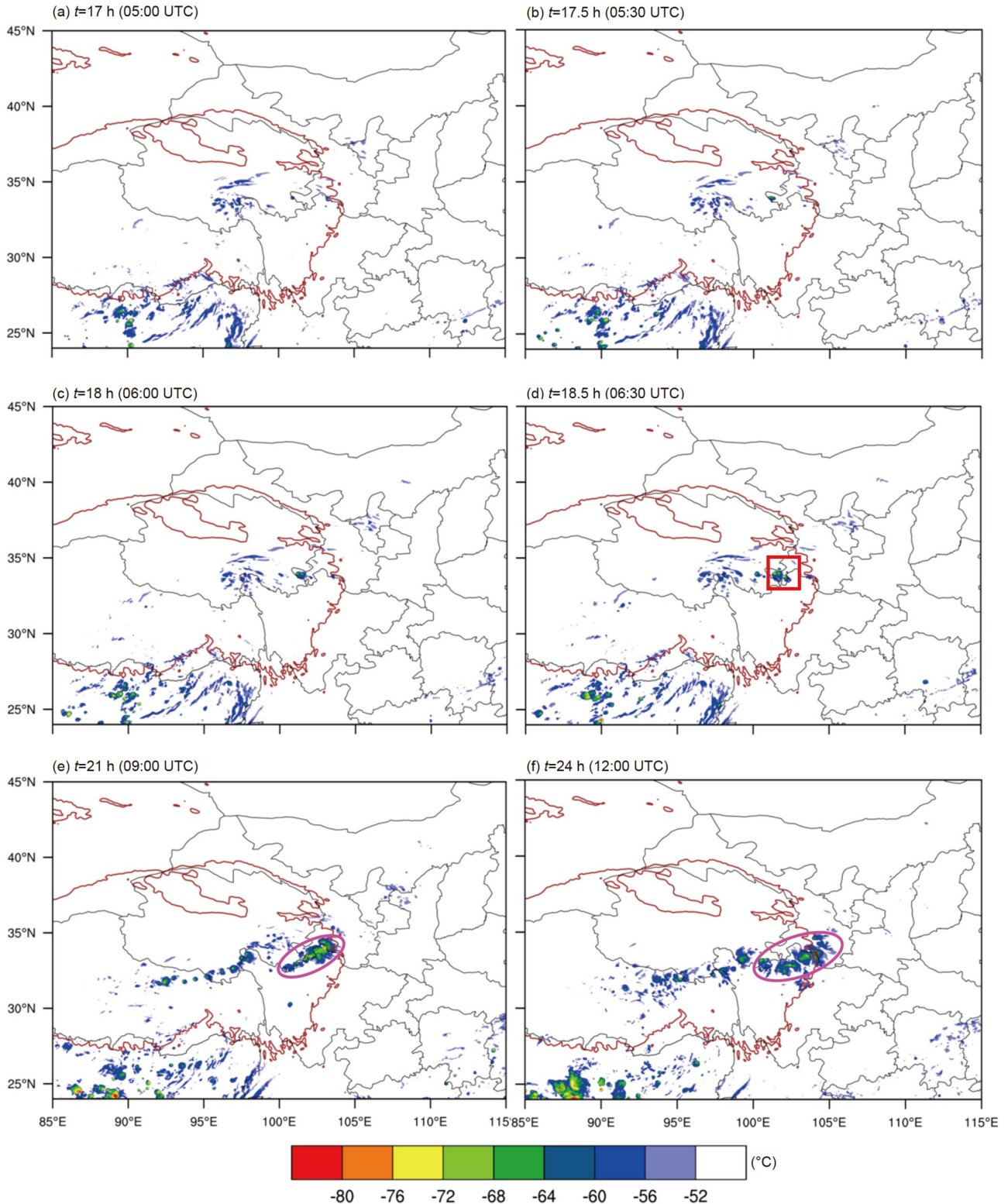
Figure 5   The control-run simulated TBB (shading, units: °C) during the formation and initial developing stages of the EVT, where the brown line shows the terrain above 3000 m, the red box marks the key region where the EVT formed, and the purple ellipses mark the focused EVT.

the box as the key region of the EVT's formation. In the upper troposphere, this box was located within a divergent upper-level region south of the 200-hPa upper-level jet (Figure 7a), which was conducive to the development of convection. In the middle troposphere, the key region was situated within the central area of the shortwave trough over the eastern section of the TP (Figures 6a and 7b), where it was governed by cyclonic vorticity and warm advection
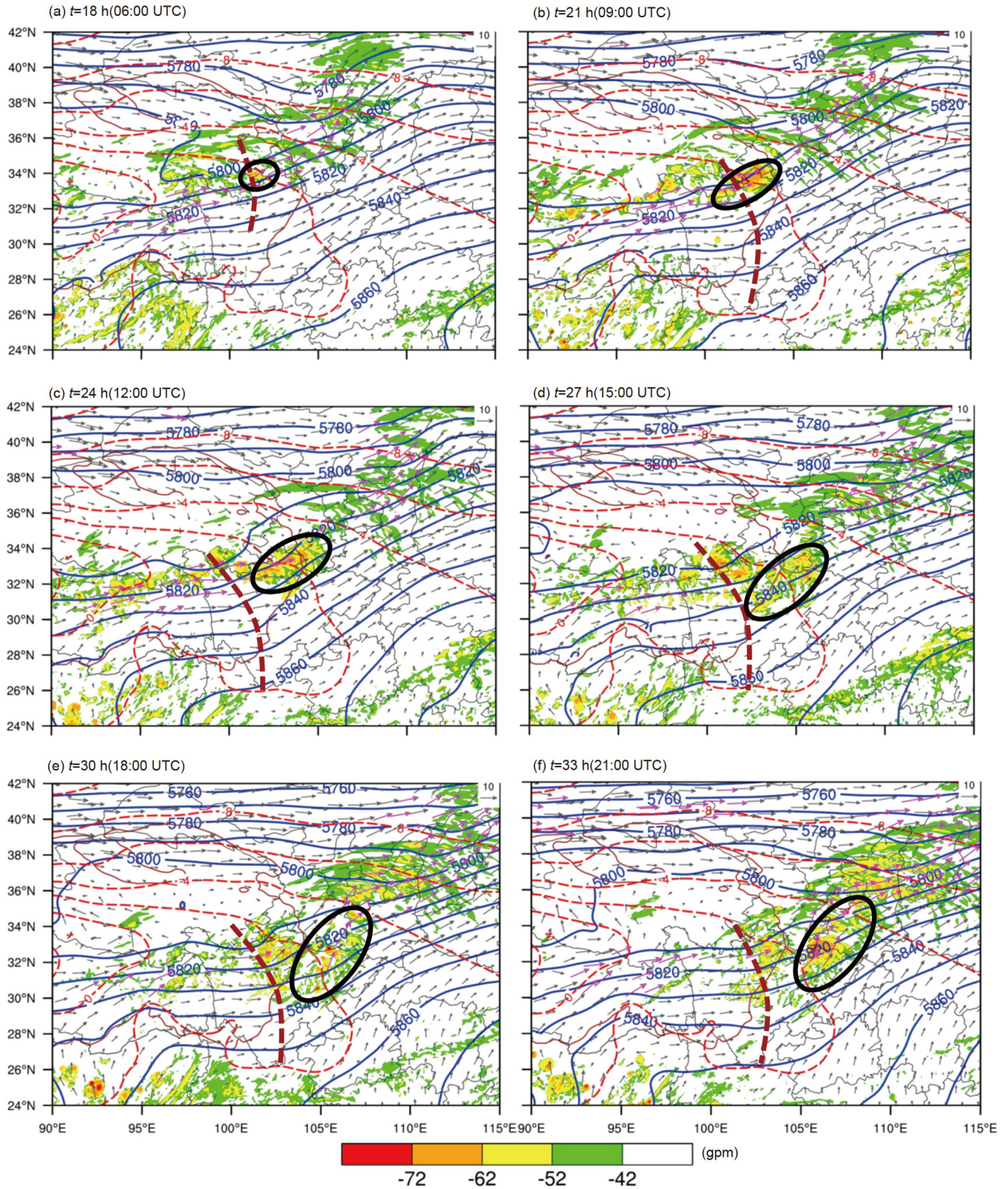
Figure 6 The control-run simulated TBB (shading, units: °C), 500 hPa geopotential height (blue solid lines, units: gpm), temperature (red dashed lines, units: gpm), and wind vector (purple vectors mark the wind speed above 12 m s^{-1}), where the brown line shows the terrain above 3,000 m, brown dashed lines are trough lines, and the black ellipses mark main body of the focused EVT.

(mainly due to strong westerly wind). According to quasi-geostrophic theory, the warm advection was favorable for promoting ascending motions (Ding, 2005), and it also contributed to pressure lowering (Fu et al., 2017, 2019), both
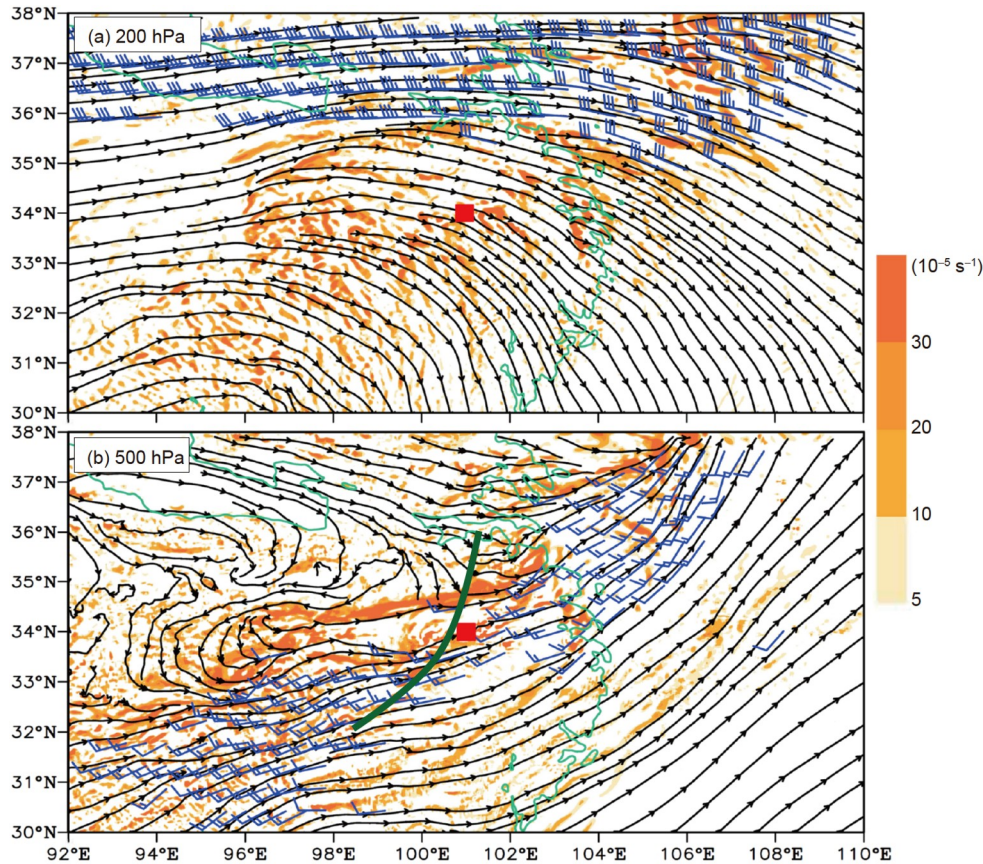
Figure 7 (a) 200 hPa stream field, divergence (shading, units: 10^{-5} s^{-1}), and wind above 30 m s^{-1} (blue wind bar, a full bar is 10 m s^{-1}); (b) 500 hPa stream field, vorticity (shading, units: 10^{-5} s^{-1}), and wind above 12 m s^{-1} (blue wind bar, a full bar is 10 m s^{-1}). Green solid line marks the terrain of 3,000 m, small red boxes show the central locations of the EVT formation, and the thick green line is the trough line.

of which acted as advantageous conditions for the EVT's formation.

As Figure 8a shows, before the EVT's formation (from *t*= 16 h (04:00 UTC) to 18.5 h (06:30 UTC)), lower levels (below 500 hPa) of the key region showed a weak convective unstable feature, with a nearly neutral stratification located above it. The lower-level unstable stratification stretched upward with time, whereas the middle-level neutral stratification shrank simultaneously. This means that convective unstable energy in the middle and lower troposphere was increasing. In the meanwhile, the cloud water experienced an increase at the levels below 500 hPa (Figure 8c), and the thickness of the layer with cloud water mixing ratio above 1×10^{-2} g kg^{-1} extended upward with time, which reflected the developing of convective clouds. For the dynamic fields, before 05:15 UTC, weak divergence, cyclonic vorticity (Figure 8b) and ascending motions (Figure 8a) dominated lower-levels (below 500 hPa) of the key region, all of which means that convection was weak in this stage. From 05:15 UTC to 06:30 UTC, the lower-level convergence and cyclonic vorticity enhanced in intensity and extended upward (Figure 8b). In the meanwhile, ascending motions in the layer of 600–200 hPa also intensified rapidly (Figure 8a),

with its maximum center appeared around 350 hPa. This means that convection developed quickly in this stage, which corresponded to the EVT's formation.

As the EVT's formation was accompanied by rapid enhancement of cyclonic vorticity, we conducted a vorticity budget to determine the key factors governing the formation process. The calculation indicates that, within the key region, vorticity of the levels below 450 hPa changed slowly before 05:15 UTC, and then from 05:15 UTC to 06:30 UTC (when the EVT formed), cyclonic vorticity enhanced rapidly (Figure 8b). Mechanisms governing the increase of cyclonic vorticity featured layer wise features (Figure 9): for the levels below 550 hPa, convergence-related STR and convection-related TIL were dominant factors for the cyclonic-vorticity production (Figure 9a and 9b). In the meanwhile, HAV was negative, implying that the horizontal transport caused a net export of cyclonic vorticity from the key region. This decelerated the increase of cyclonic vorticity, which was detrimental for the EVT's formation. The effect of VAV was also negative (Figure 9d), implying that convection mainly transported cyclonic vorticity below 550 hPa to the levels above (as Figure 8a, 8b shown, ascending motions and cyclonic vorticity dominated the key region at levels below
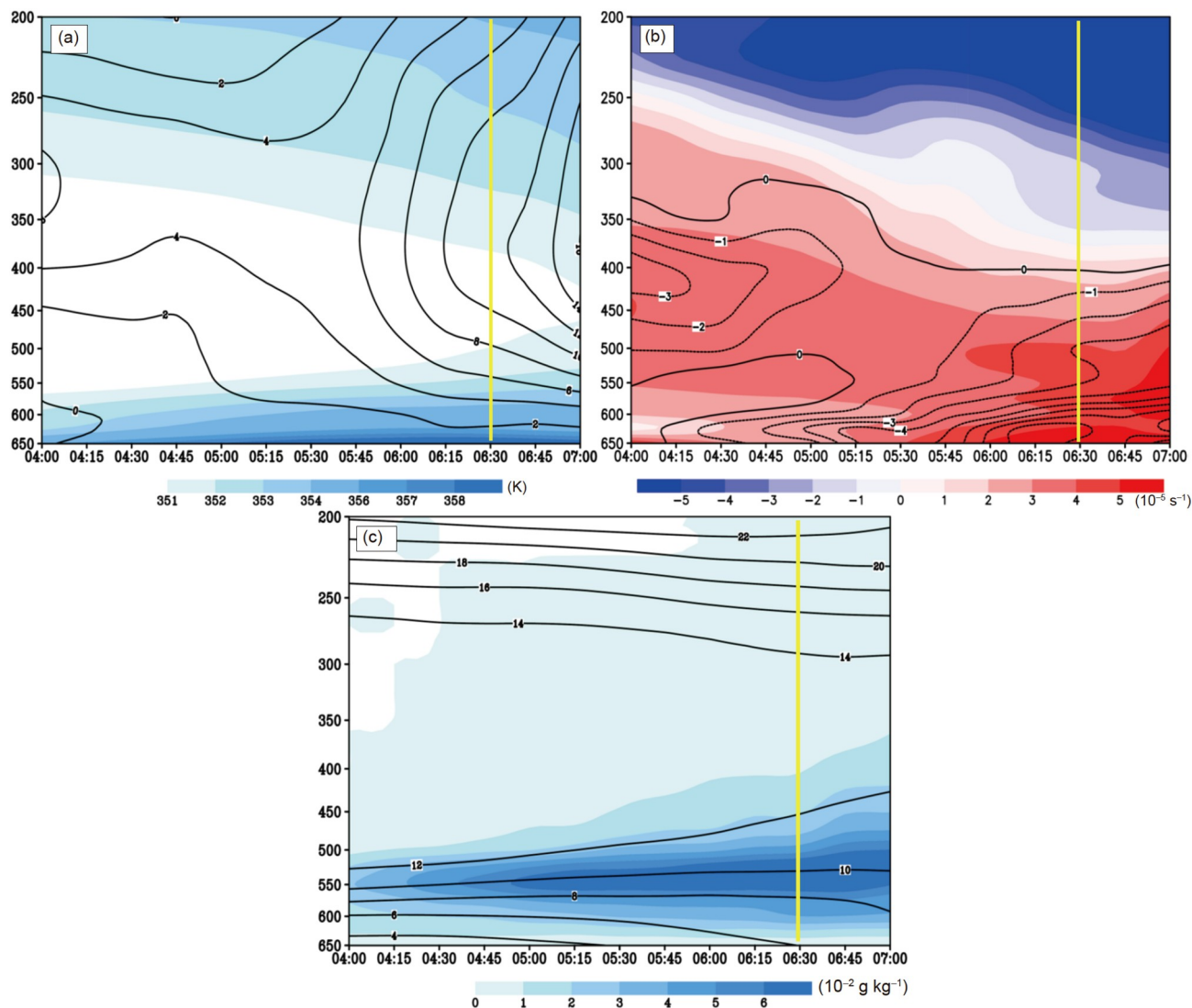
Figure 8 (a) The key region (Figure 5d) averaged pseudo-equivalent potential temperature (shading, units: K) and vertical wind speed (black lines, units: cm s^{-1}). (b) The key region averaged vorticity (shading, units: 10^{-5} s^{-1}) and divergence (black lines, units: 10^{-5} s^{-1}). (c) The key region averaged cloud water mixing ratio (shading, units: 10^{-2} g kg^{-1}) and horizontal wind speed (black lines, units: m s^{-1}). The yellow solid lines mark the time when the EVT formed, *x*- and *y*-axis are time (UTC) and pressure (units: hPa), respectively.

550 hPa). For the levels between 550 and 450 hPa, cyclonic vorticity within the key region enhanced mainly through HAV and VAV (Figure 9c, 9d), whereas, STR and TIL mainly acted in an opposite manner (Figure 9a, 9b). Overall, vertical transport (VAV) was the most favorable factor for the cyclonic-vorticity increase (Figure 9d). It should be noted that, from 5:45 UTC on, VAV enhanced notably in the layer of 550–200 hPa, implying that strong convection (Figure 8a) transported the cyclonic vorticity produced by STR and TIL in the lower levels to the higher levels. This was conducive to the EVT's upward stretching.

4.2 Vacating and redeveloping stages

4.2.1 Vacating stage

After formation, the EVT intensified and moved eastward

with time, and by *t*=24 h, it began to vacate the TP. Around this time, within the main body of EVT, convective unstable stratification (Figure 10a) accompanied by strong convergence (Figure 10d) appeared in the levels below 550 hPa. Between 550 hPa and 300 hPa, there was an approximately neutral stratification (Figure 10a), which was the result of convection. Due to latent heat release, several columns with strong positive potential vorticity (PV) (exceeding 2 PVU or even 3 PVU) was generated in the layer. In contrast, levels above 300 hPa were mainly stable (Figure 10a). Ascending motions appeared in the layer from the surface to 200 hPa (Figure 10b), with its strongest center located around 300 hPa. Ahead of the EVT, there were strong unstable stratification, convergence zone and positive PV columns (due to latent heating) in the lower and middle troposphere (Figure 10a and 10d), all of which acted as favorable conditions for
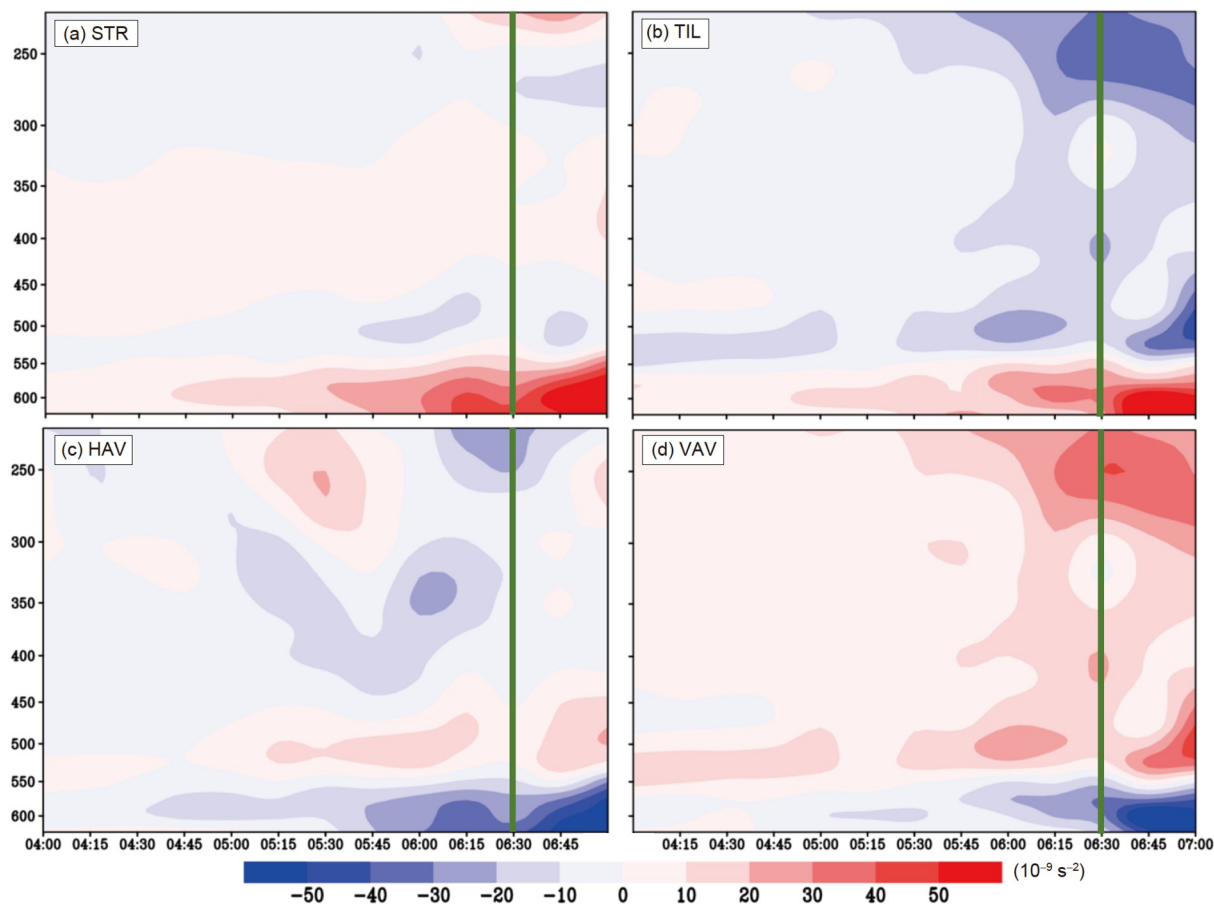
Figure 9   Key region (Figure 5d) averaged STR (a), TIL (b), HAV (c), VAV (d), respectively (shading, units: $10^{-9}\,\mathrm{s}^{-2}$). The green solid lines mark the time when the EVT formed, *x*- and *y*-axis are time (UTC) and pressure (units: hPa), respectively.

the maintenance of the EVT after its vacating. During the vacating stage (from 24 to 29 h), lower layer (650–550 hPa) of the EVT featured decreasing convergence and lowering pseudo-equivalent potential temperature (cf., Figure 10a, 10b and 10d, 10e), which was mainly due to the weakening of direct sensible heating (from the TP) on the bottom of the EVT. In this stage, ascending motions and positive PV in the whole layer (from surface to 200 hPa) mainly reduced in intensity, implying the weakening of the EVT. Compared with previous studies, we found that the results mentioned above were consistent with (i) the common evolutionary features of the EVTs derived from a 16-warm-season statistical study (Mai et al., 2021); and (ii) the evolutionary mechanisms governing a simulated EVT during its vacating stage (Fu et al., 2019). After the EVT completely moved out from the TP, it was mainly located ahead of the shortwave trough over the eastern section of the TP (Figure 6e), where dynamical conditions were favorable. Merging of the EVT-associated attributions with local ones east of the TP (including the positive PV columns in the whole layer, and the convergence zone and neutral stratification in the middle troposphere) notably enhanced the convergence in the middle and lower troposphere, and the ascending motions and

positive PV columns in the whole layer (Figure 10c and 10f). Due to the above, the EVT was redeveloped again.

Variation of the EVT was closely related to a quasi-stationary TPV (Figure 11) that was maintained over the eastern section of the TP (32.5°–36.5°N, 100.5°–104.5°E, which was defined as the central region of the vortex). This vortex formed ~4.5 h latter than that of the EVT (*t*=23 h), when ascending motions with the central region was weakening (Figure 12a). Therefore, the formation of the TPV was a result of convective activities over the TP (consistent with the vorticity budget results shown below). When the TPV formed, it was coupled with the central area of the EVT (Figure 11a). This was conducive to the maintenance of both EVT and TPV through sustaining ascending motions and convergence in the middle and lower troposphere. Then, the EVT moved eastward relative to the TPV, and from *t*=25 h on, it began to uncouple from the vortex (Figure 11b). By *t*= 29 h, the EVT's main body had completely vacated the TP and separated from the TPV (Figure 11d). One hour later (*t*= 30 h), the TPV dissipated. As the temporal mean (from the TPV's formation to its dissipation) 500-hPa wind field indicates, weak northerly and strong southerly wind dominated the western and eastern sections of the TPV, respectively,
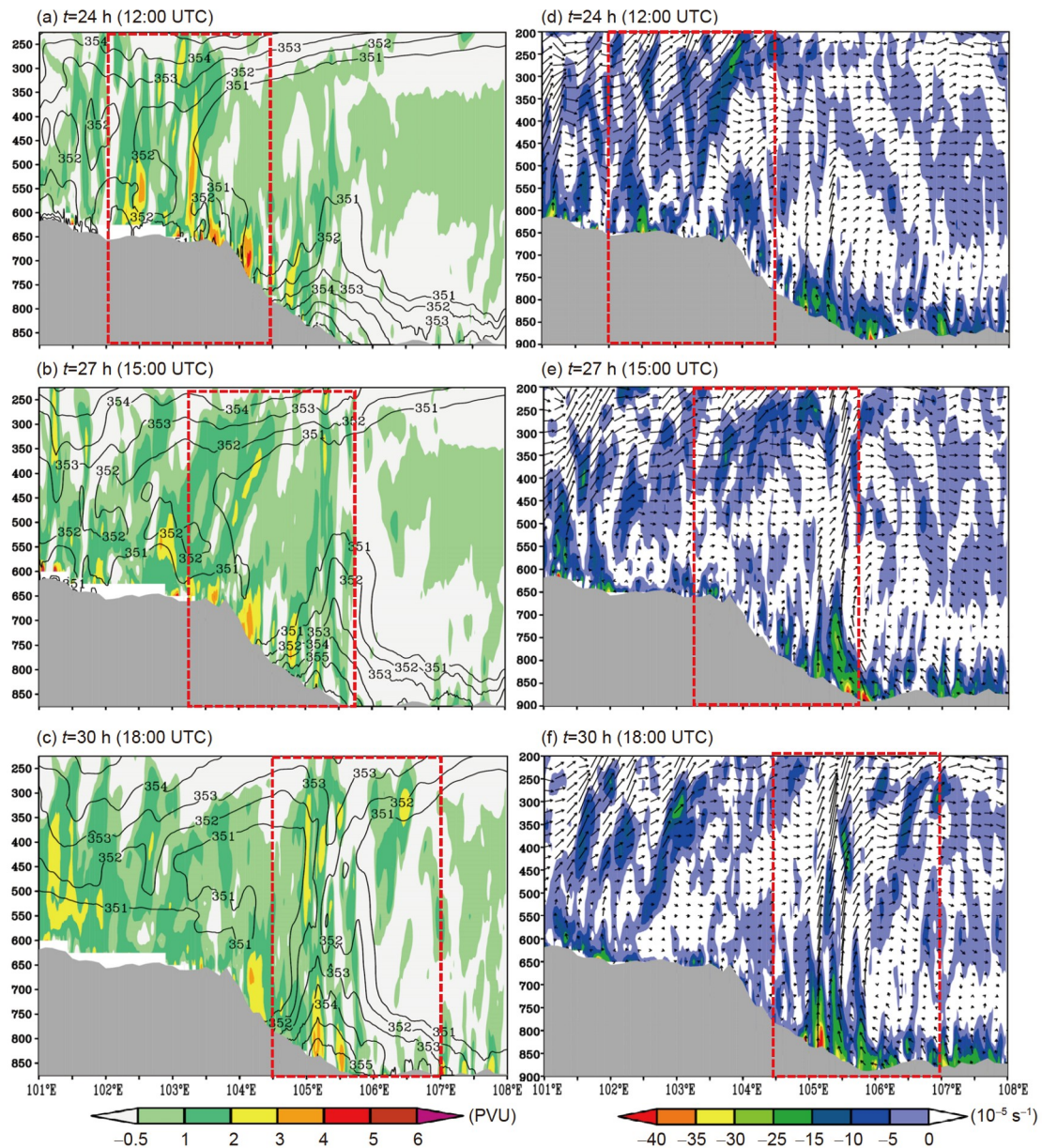
Figure 10 (a)–(c) show the meridional average (32°–34°N) potential vorticity (shading, units: PVU) and pseudo-equivalent potential temperature (black solid lines, units: K). (d)–(f) show the meridional average (32°–34°N) divergence (shading, units: 10^{-5} s^{-1}) and composite of zonal wind (units: m s^{-1}) and vertical wind (units: cm s^{-1}). All data are from the output of control run, the grey shading area shows the meridional average (32°–34°N) terrain, and the red dashed boxes mark the main body of the EVT.

whereas zonal wind was small (not shown). This was a key reason why the vortex kept a quasi-stationary behavior during its lifespan.

Vorticity budget averaged within the central region of the TPV (blue boxes in Figure 11) was used to understand its evolutionary mechanisms. As Figure 12a and 12b show, from 09:00 UTC to 11:00 UTC, central region of the TPV experienced a rapid increase of cyclonic vorticity, which corresponded to the TPV's formation. Upward transport of cyclonic vorticity (VAV) and convergence-related vertical stretching (STR), both of which were closely related to convective activities over the TP, acted as the first and sec-

ond dominant factors for the vortex's formation (Figure 12c, 12d). Life span of the TPV could be roughly divided into two stages: (i) 11:00–13:00 UTC, during which the vortex was coupling with the EVT (Figure 11a, 11b); and (ii) 14:00–17:00 UTC, when the vortex was decoupling from the EVT (Figure 11c, 11d). The key reason for the decoupling was that the westerly-wind steering flow was much stronger for the EVT than that of the TPV (not shown), which made the former move much faster. Displacement of the EVT relative to the TPV finally resulted in their decoupling. As Figure 12a, 12b illustrate, during the coupling stage, term TOT was positive around 500 hPa (525–475 hPa) of the central region
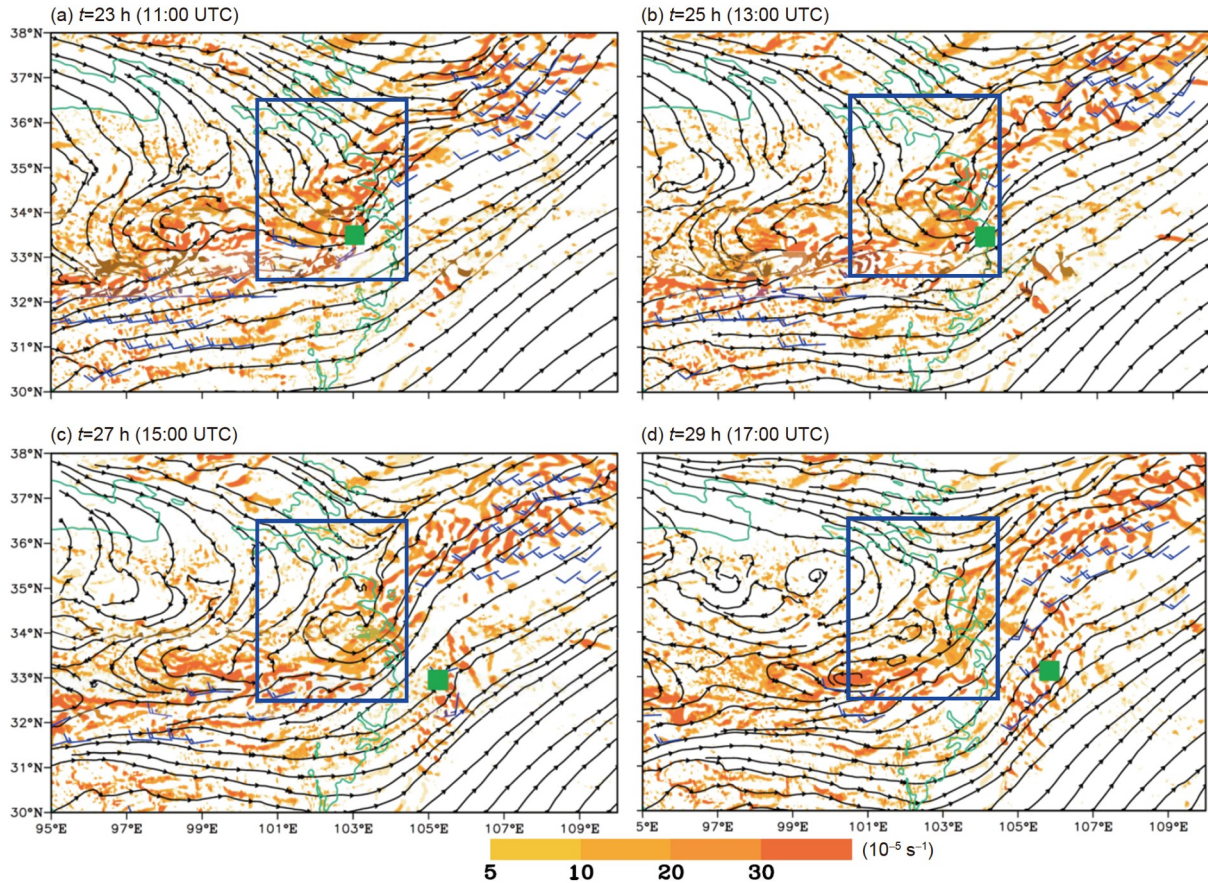
Figure 11 The 500 hPa stream field, vorticity (shading, units: 10^{-5} s^{-1}), and wind above 12 m s^{-1} (a full bar is 10 m s^{-1}), where the green solid line marks the terrain of 3,000 m, the blue rectangles show the central region of the TPV, and the green boxes mark the center of the EVT.

of the TPV (Figure 12b), which contributed to the vortex's maintenance. Of these, the horizontal (Figure 12e) and upward transports (Figure 12d) of cyclonic vorticity were governing factors for the vortex's sustainment (from Figure 12a, convection was strong in this stage), whereas other budget terms mainly showed negative effects. During the decoupling stage, TOT around 500 hPa (525–475 hPa) became negative (Figure 12b), which indicates that the TPV began to weaken. Notable weakening of vertical cyclonic-vorticity transport (as Figure 12a shown, convection weakened remarkably in this stage) was the main reason for term TOT's change from positive to negative. In addition, the anticyclonic vorticity production due to tilting (TIL) was another reason for the TPV's weakening and dissipation (Figure 12f). In contrast, the horizontal transport of vorticity (mainly due to the net import transport of cyclonic vorticity by the southwesterly wind that originated from the regions southwest of the TPV) decelerated the vortex's dissipation (Figure 12e).

4.2.2 Redeveloping stage
After vacating the TP, the EMT first weakened in intensity (Section 4.2.1). In this stage, the term TOT was weakly negative in the middle and lower troposphere (below 400 hPa) of the EVT (not shown). From t=30 h (18:00 UTC) to 33 h (21:00 UTC), the EVT redeveloped rapidly (Figure 6e, 6f). This corresponded to a rapid increase of convergence in the lower troposphere, and a quick intensification of positive PV and ascending motions in the whole layer (see the features within the red dashed boxes of Figure 10b, 10c, 10e, and 10f). Strong condensation latent heating, on the one hand, enhanced the positive feedback among convergence, ascending motion and latent heating (Raymond and Jiang, 1990), which intensified convection; and on the other hand, it contributed to the EVT's development and maintenance through producing positive PV anomaly that was associated with cyclonic wind perturbation and negative geopotential-height perturbation (Fu et al., 2019).

Figure 3 illustrates the key area (31°–35°N, 105°–109°E) averaged vorticity budget during the redeveloping stage of the EVT. It can be found that, before the EVT's redeveloping (t=30 h), at middle and lower levels (below 400 hPa) of the key area, cyclonic vorticity showed increasing and decreasing tendencies alternately, rather than a consistent rapid increasing trend. Correspondingly, convective activities within
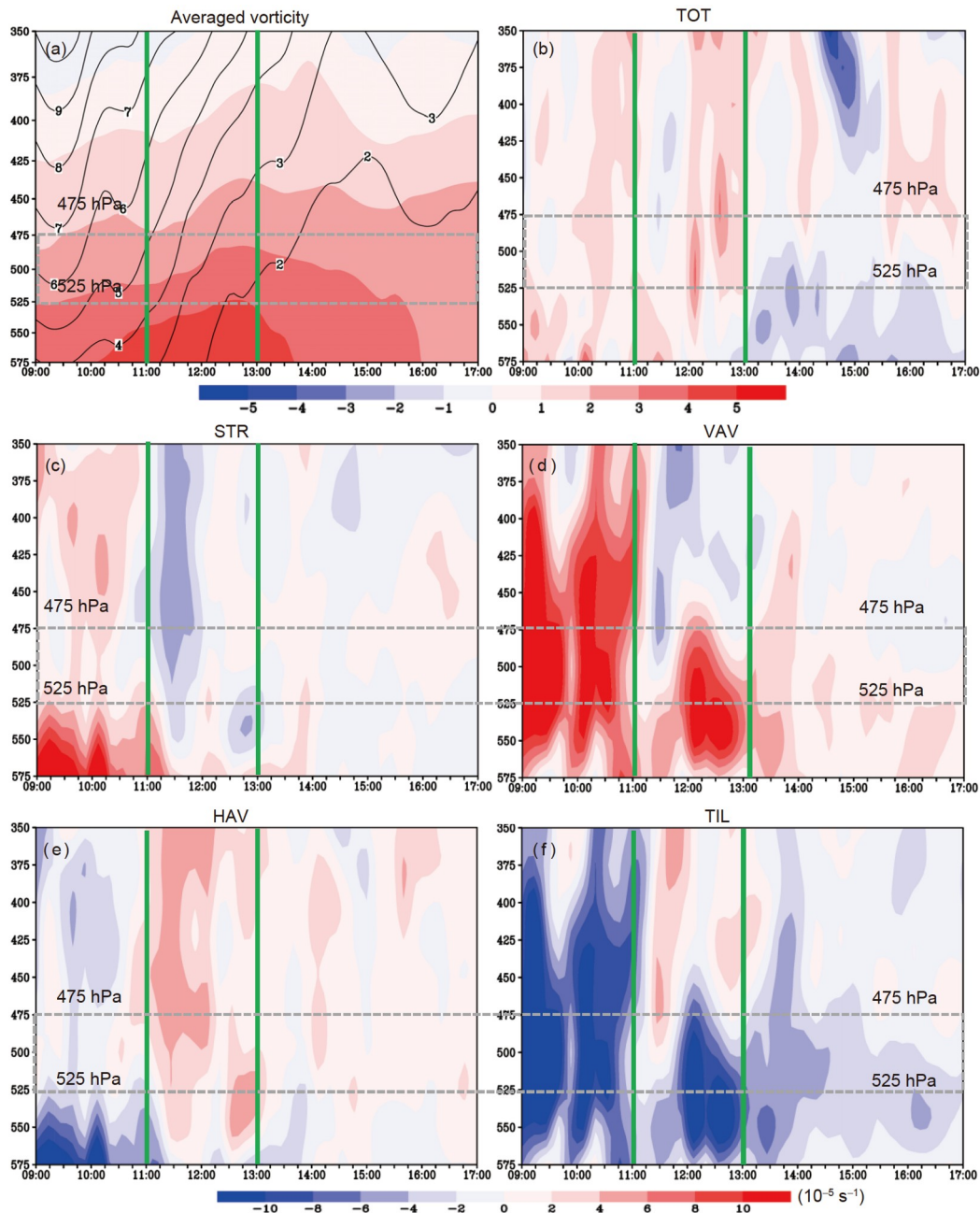
Figure 12 (a) The area (central region of the TPV) averaged vorticity (shading, units: 10^{-5} s^{-1}) and vertical wind speed (black lines, units: m s^{-1}). (b)–(f) The area averaged vorticity budget terms, respectively (shading, units: 10^{-9} s^{-2}). The green solid lines mark the typical time, *x*- and *y*-axis are time (UTC) and pressure (units: hPa), respectively.

this area also were also alternate (not shown). During this period, the term VAV was the dominant factor for the increase of cyclonic vorticity within the key area (Figure 13d). When entering the redeveloping stage (from *t*=30 h to 33 h), a strong positive TOT appeared at middle and lower levels (below 400 hPa) of the key area (Figure 13e), which implies that cyclonic vorticity was increasing rapidly. In the meanwhile, ascending motions also strengthened quickly (not shown). Convergence-related vertical stretching (Figure 13a) and upward transport of cyclonic vorticity (Figure 13d)

controlled the EVT's redeveloping, whereas tilting (Figure 13b) and horizontal transport (Figure 13c) mainly decelerated the process.

4.2.3 Sensitivity simulation analyses
From the analysis above, it is clear that: (i) condensation latent heating was critical to the EVT's development and sustainment; and (ii) EVT affected the downstream precipitation east of the TP notably. These two phenomena were investigated by using a NOLH sensitivity simulation that
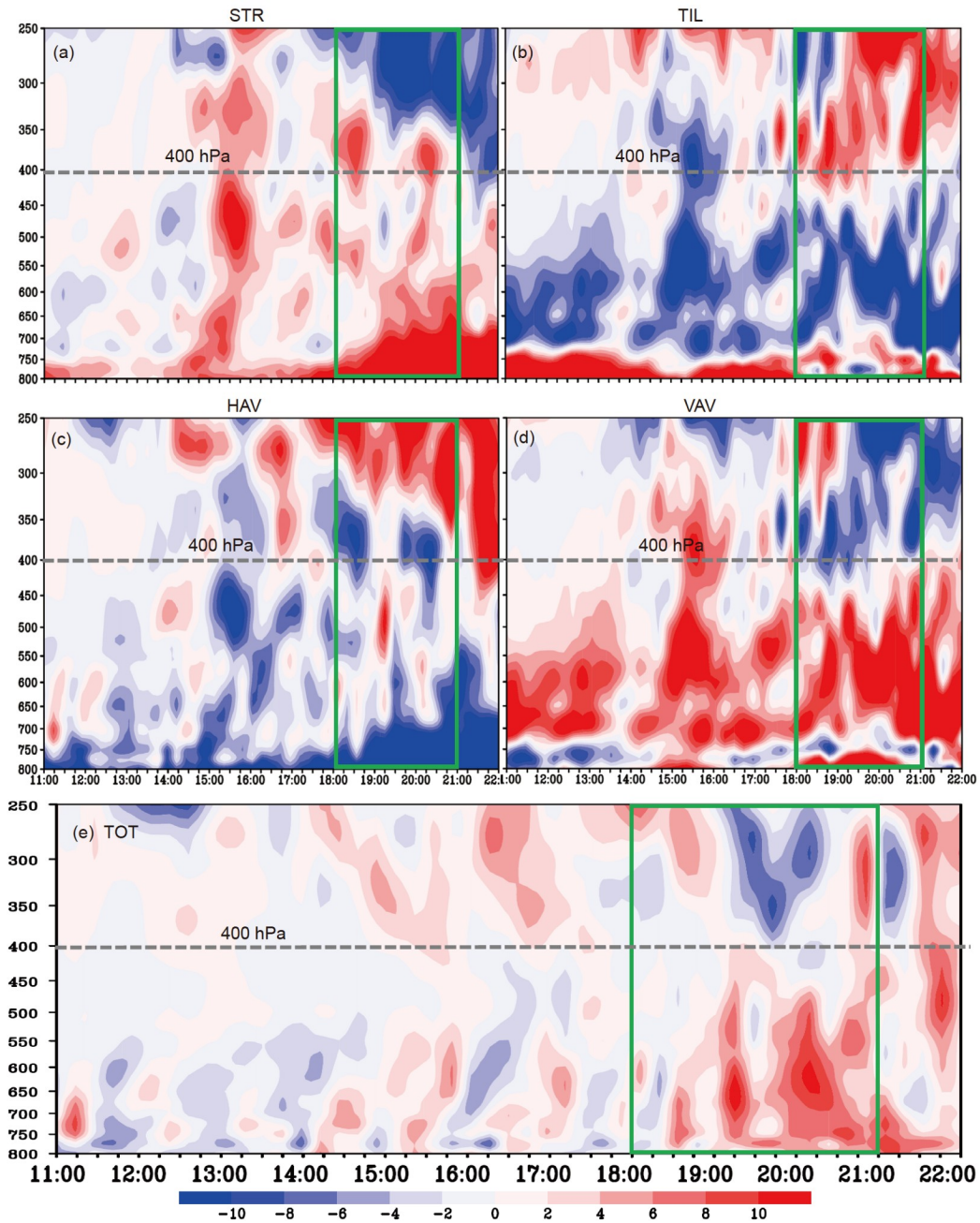
Figure 13   Key area (of redeveloping) averaged STR (a), TIL (b), HAV (c), VAV (d), and TOT (e), respectively (shading, units: 10^{-9} s^{-2}). The green solid lines mark the period when the EVT redeveloped, *x*- and *y*-axis are time (UTC) and pressure (units: hPa), respectively.

switched latent heating off over the main body of the TP (Figure 2). As Figures 6a, 6c and 14a, 14b show, after removing condensation latent heating over the TP's main body, the shortwave trough over the eastern section of the TP still appeared, but of a weaker intensity (in terms of the geopotential height of the trough and the coverage of the −2°C contour over the TP). Westerly wind around the central area of the shortwave trough weakened notably (see purple arrows in Figures 6a, 6c and 14a, 14b), and convective activities were very weak over the TP (Figure 14a, 14b). Only scattered convective clouds appeared in front of the trough,

with some of them reaching a minimum TBB of below −52°C. However, none of them had reached the lower aera limit of an MCS (≥5000 km^2). Furthermore, in some downstream regions, adjustments of the background circulations appeared (e.g., the 500-hPa strong wind band weakened over Ninxia Autonomous Region, the wind and geopotential height fields changed over the border of Provinces Sichuan, Yunnan and Guizhou, etc.). In the NOLH run, no EVT formed from *t*=0 h to 24 h, whereas, during the same period, the control-run EVT had already experienced formation, development and vacating (Figure 6c). This sharp contrast
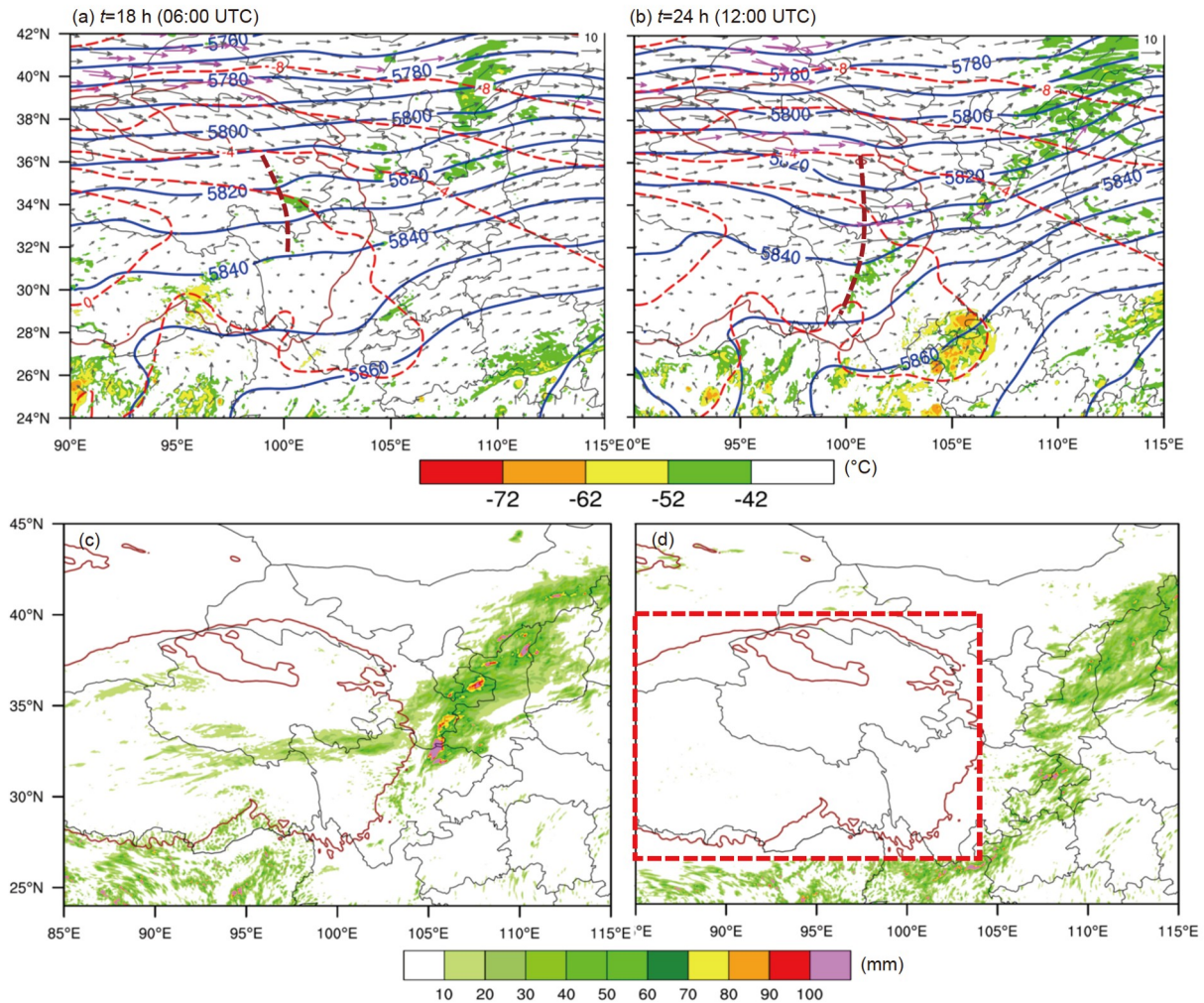
Figure 14   (a), (b) The NOLH-run simulated TBB (shading, units: °C), 500 hPa geopotential height (blue solid lines, units: gpm), temperature (red dashed lines, units: gpm), and wind vector (purple vectors mark the wind speed above 12 m s^{-1}), where the brown line shows the terrain above 3,000 m, and brown dashed lines are trough lines. (c) The control-run simulated accumulated (from t=18.5 h to 47 h) precipitation (shading, units: mm), where the brown line shows the terrain above 3,000 m. (d) The same as (c), but for the NOLH run (the red dashed box marks the region removing latent heating).

indicates that condensation latent heating was a necessary condition for the EVT's formation and development. The comparison between Figure 14c and 14d shows that removing condensation latent heating over the TP's main body reduced the precipitation over the TP notably, as convective activities became much weaker. Moreover, precipitation over the downstream regions east of the TP had been greatly adjusted: (i) the precipitation center over the junction of Provinces Sichuan, Gansu, and Shaanxi was remarkably weakened, as there was no EVT (i.e., direct influence of the EVT was removed); (ii) the precipitation over northern Shaanxi decreased, whereas, that over northern Yunnan, northwestern Guizhou, Chongqing and Shanxi increased. This indicates that the EVT could indirectly affect the precipitation over wider downstream regions by modulating the background circulations over and around the TP (Fu et al., 2019).

5.   Conclusion and discussion

In this study, based on an objective standard, we selected 11 long-lived EVTs of the same type from the statistical results of MCSs (that were generated over the TP) during a 16-warm-season period. The composite of these 11 EVTs was used to drive the WRF model for a semi-idealized simulation. Evolutionary features and associated governing mechanisms of this type of long-lived EVT were investigated from the perspective of commonness. In addition, a NOLH sensitivity simulation was used to show the influences of the EVT on the precipitation over the TP and in downstream regions.

During the EVT's formation stage, a favorable vertical configuration in background environment was found around its formation location: In the upper troposphere, there was divergence associated with an upper-level jet (that was

mainly located between 35°N and 45°N); in the middle troposphere, there was warm advection associated with a shortwave trough over the eastern section of the TP; and in the lower troposphere, there was strong convergence and notable convective instability. The EVT's formation process featured an increase in cyclonic vorticity, and the vorticity budget indicates that convergence-related STR and convection-related TIL were dominant factors for producing cyclonic vorticity, and the vertical transport of cyclonic vorticity due to convection contributed to the EVT's upward extending.

During the eastward moving stage of the EVT, it experienced the coupling and decoupling processes with a quasi-stationary TPV over the eastern section of the TP. In the former process, the EVT was helpful to maintain the convergence and ascending motions associated with the vortex, which made terms STR and VAV act as the two dominant factors for the formation and sustainment of the TPV. In the latter process, as the EVT vacated the TP, it decoupled from the TPV, which significantly reduced the intensity of ascending motions associated with the vortex. Correspondingly, the upward transport of cyclonic vorticity weakened notably, which, together with the strong negative tilting effect, finally resulted in the TPV's dissipation.

During the stage after EVT's vacating, as the sensible direct heating from the TP on its bottom disappeared, the EVT first weakened in intensity. Then, under the favorable conditions associated with the shortwave trough over the TP's eastern section, the EVT merged with several local convective clouds and redeveloped rapidly. Vorticity budget shows that convergence-related STR (at middle and lower levels) and convection-related upward transport of cyclonic vorticity (VAV) dominated the EVT's redevelopment. In contrast, terms TIL and HAV mainly decelerated this process.

Condensation latent heating was a necessary condition for the formation and development of the long-lived EVT. The EVT exerted a notable effect on the precipitation over the TP's eastern section and the regions east of the plateau. On the one hand, the EVT could directly induce precipitation over these regions. On the other hand, it could affect the precipitation over a wider area by modulating the large-scale background circulations over the TP and its surrounding regions.

References

Chen F, Dudhia J. 2001. Coupling an advanced land surface-hydrology model with the Penn State-NCAR MM5 modeling system. Part I: Model implementation and sensitivity. Mon Wea Rev, 129: 569–585

Ding Y H. 2005. Advanced Synoptic Meteorology (in Chinese). Beijing: China Meteorological Press. 585

Dudhia J. 1989. Numerical study of convection observed during the winter monsoon experiment using a mesoscale two-dimensional model. J Atmos Sci, 46: 3077–3107

Flohn H, Reiter E R. 1968. Contributions to a meteorology of the Tibetan Highlands. Atmospheric Science Paper No 130. Fort Collins: Colorado State University

Fu S M, Mai Z, Sun J H, Li W L, Ding Y, Wang Y Q. 2019. Impacts of convective activity over the Tibetan Plateau on plateau vortex, southwest vortex, and downstream precipitation. J Atmos Sci, 76: 3803–3830

Fu S M, Sun J H, Luo Y L, Zhang Y C. 2017. Formation of long-lived summertime mesoscale vortices over central east China: Semi-idealized simulations based on a 14-year vortex statistic. J Atmos Sci, 74: 3955–3979

Fu S M, Sun J H, Zhao S X, Li W L. 2010. The impact of the eastward propagation of convective systems over the Tibetan Plateau on the southwest vortex formation in summer. Atmos Ocean Sci Lett, 3: 51–57

Fu S M, Sun J H, Zhao S X, Li W L, Li B. 2011. A study of the impacts of the eastward propagation of convective cloud systems over the Tibetan Plateau on the rainfall of the Yangtze-Huai River basin (in Chinese). Acta Meteor Sin, 69: 581–600

Fu S M, Yu F, Wang D H, Xia R D. 2013. A comparison of two kinds of eastward-moving mesoscale vortices during the mei-yu period of 2010. Sci China Earth Sci, 56: 282–300

Hong S Y, Lim J O. 2006. The WRF single-moment microphysics scheme (WSM6). J Korean Meteor Soc, 42: 129–151

Hu L, Deng D, Gao S, Xu X. 2016. The seasonal variation of Tibetan convective systems: Satellite observation. J Geophys Res Atmos, 121: 5512–5525

Hu L, Deng D, Xu X, Zhao P. 2017. The regional differences of Tibetan convective systems in boreal summer. J Geophys Res Atmos, 122: 7289–7299

Joyce R J, Janowiak J E, Arkin P A, Xie P. 2004. CMORPH: A method that produces global precipitation estimates from passive microwave and infrared data at high spatial and temporal resolution. J Hydrometeor, 5: 487–503

Kain J S. 2004. The Kain-Fritsch convective parameterization: An update. J Appl Meteor, 43: 170–181

Kirk J R. 2003. Comparing the dynamical development of two mesoscale convective vortices. Mon Wea Rev, 131: 862–890

Li G P, Xu Q. 2005. Effect of dynamic pumping in the boundary layer on the Tibetan Plateau vortices (in Chinese). Chin J Atmos Sci, 29: 965–972

Li Y D, Wang Y, Yang S, Hu L, Gao S T, Fu R. 2008. Characteristics of summer convective systems initiated over the Tibetan Plateau. Part I: Origin, track, development, and precipitation. J Appl Meteor Climatol, 47: 2679–2695

Liu Y M, Lu M M, Yang H J, Duan A M, He B, Yang S, Wu G X. 2020. Land-atmosphere-ocean coupling associated with the Tibetan Plateau and its climate impacts. Natl Sci Rev, 7: 534–552

Mai Z, Fu S M, Sun J H, Hu L, Wang X M. 2021. Key statistical characteristics of the mesoscale convective systems generated over the Tibetan Plateau and their relationship to precipitation and southwest vortices. Int J Climatol, 41: E875–E896

Mlawer E J, Taubman S J, Brown P D, Iacono M J, Clough S A. 1997. Radiative transfer for inhomogeneous atmospheres: RRTM, a validated correlated-k model for the longwave. J Geophys Res, 102: 16663–16682

Noh Y, Cheon W G, Raasch S. 2001. The improvement of the K-profile model for the PBL using LES. In: Preprints of the International Workshop of Next Generation NWP Model. Seoul, South Korea. 65–66

Raymond D J, Jiang H. 1990. A theory for long-lived mesoscale convective systems. J Atmos Sci, 47: 3067–3077

Saha S, Moorthi S, Wu X, Wang J, Nadiga S, Tripp P, Behringer D, Hou Y T, Chuang H, Iredell M, Ek M, Meng J, Yang R, Mendez M P, van den Dool H, Zhang Q, Wang W, Chen M, Becker E. 2014. The NCEP climate forecast system version 2. J Clim, 27: 2185–2208

Skamarock W C, Klemp J B, Dudhia J, Gill D O, Barker D M, Duda M G, Huang X Y, Wang W, Powers J G. 2008. A description of the Advanced Research WRF version 3. NCAR Tech. Note CAR/TN-475+STR, 113

Yanai M, Li C F, Song Z S. 1992. Seasonal heating of the Tibetan Plateau and its effects on the evolution of the Asian summer monsoon. J Meteorol Soc Jpn, 70: 319–351

Yang W Y, Ye D Z, Wu G X. 1992. The influence of the Tibetan Plateau on the thermal and circulation fields over east Asia in summer II: Main features of the local circulation fields and the large scale vertical circulation fields (in Chinese). Chin J Atmos Sci, 16: 287–301

Yasunari T, Miwa T. 2006. Convective cloud systems over the Tibetan Plateau and their impact on meso-scale disturbances in the Meiyu/Baiu frontal zone. J Meteorol Soc Jpn, 84: 783–803

Ye D Z, Gao Y X. 1979. The Meteorology of Qinghai-Xizang (Tibet) Plateau (in Chinese). Beijing: Science Press. 278

Yi Q J, Xu X D. 2001. The propagation and development of cloud cluster systems and severe precipitation event in 1998. Clim Environ Res, 6: 139–145

Zhang S L, Tao S Y. 2002. The influences of Tibetan Plateau on weather anomalies over Changjiang River in 1998 (in Chinese). Acta Meteor Sin, 60: 442–452

Zhao S X, Tao Z Y, Sun J H, Bei N F. 2004. Study on Mechanism of Formation and Development of Heavy Rainfalls on Meiyu Front in Yangtze River (in Chinese). Beijing: China Meteorological Press. 282

Zheng Y G, Chen J, Zhu P J. 2008. Distribution and diurnal variation characteristics of mesoscale convective system in China and its surrounding areas in summer (in Chinese). Chin Sci Bull, 4: 471–481

Zhu G F, Chen S J. 1999. Convective activities over the Qinghai-Xizang Plateau and adjacent Regions in summer of 1995 (in Chinese). Plateau Meteor, 18: 9–18

Zhuo G, Xu X D, Chen L S. 2002. Instability of eastward movement and development of convective cloud clusters over Tibetan Plateau (in Chinese). Chin J Appl Meteorol, 13: 448–456

(Responsible editor: Zhiping WEN)